ARTICLE

Wide-Temperature Butyronitrile-Based Electrolyte: Structure Dynamics and Solvation Behavior†

Lin Tong[a,b], Juan Zhao[a,b*], Jianping Wang[a,b*]

a. Beijing National Laboratory for Molecular Sciences, CAS Research/Education Center for Excellence in Molecular Sciences, Molecular Reaction Dynamics Laboratory, Institute of Chemistry, Chinese Academy of Sciences, Beijing 100190, China
b. University of Chinese Academy of Sciences, Beijing 100049, China

(Dated: Received on July 25, 2025; Accepted on November 3, 2025)

Due to their high dielectric constant, low melting point, and high boiling point, nitrile-based solvents exhibit significant potential in wide-temperature-range electrolytes. In this study, a wide-temperature electrolyte system composed of lithium bis(trifluoromethanesulfonyl)imide (LiTFSI), dimethyl carbonate (DMC), and butyronitrile (BN) in a molar ratio of 1:3:9 was designed. Using variable-temperature infrared (IR) spectroscopy with carbonyl (C=O) and cyano (C≡N) groups as IR probes, combined with molecular dynamics simulations and density functional theory calculations, the temperature-dependent evolution of the Li^+ solvation structure and molecular dynamics were systematically investigated over the range of −45 °C to 45 °C. The results show that the introduction of BN not only significantly enhances the low-temperature ionic conductivity and high-temperature stability of the electrolyte, but also optimizes the solvation structure and interfacial characteristics of lithium ions through strong coordination interactions. This work provides both theoretical insights and experimental support for the design of wide-temperature electrolytes.

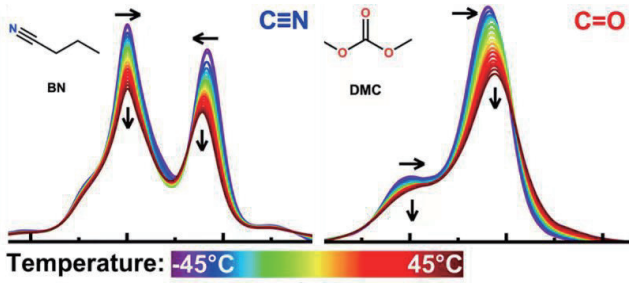

Key words: IR spectroscopy, Electrolytes, Lithium-ion batteries, Vibrational probe, Temperature dependence

I. INTRODUCTION

Lithium-ion batteries (LIBs) have been widely used in various fields, including portable electronics, electric vehicles, and energy storage systems [1–4]. With the growing diversification of usage scenarios, it is becoming more and more critical to ensure the stability and reliability of LIBs under extreme temperature conditions [5, 6]. At lower temperatures, the viscosity of electrolytes increases significantly, leading to reduced lithium salt solubility and ionic conductivity. Moreover, the kinetics of electrochemical processes, such as charge transport and lithium intercalation/deintercalation, slow down markedly, leading to substantial degradation in battery capacity, cycle performance, and safety [7–10]. Conversely, at higher temperatures, the electrolyte and the solid electrolyte interphase (SEI) become unstable, which leads to side reactions and increases the risk of thermal runaway. These issues can significantly shorten battery lifespan and pose serious safety risks [11–14]. Therefore, the development of batteries capable of stable operation over a broad tempera-

† Part of Special Issue dedicated to Professor Fanao Kong on the occasion of his 90th birthday.
* Authors to whom correspondence should be addressed.
E-mail: zhaojuan@iccas.ac.cn, jwang@iccas.ac.cn

ture range is becoming one of the key challenges in the advancement of LIBs [15–17].

As a key component of LIBs, the electrolyte not only enables lithium-ion transport but also directly influences the formation and stability of the electrode–electrolyte interface, playing a crucial role in overall battery performance [18]. Conventional electrolytes typically consist of $LiPF_6$ dissolved in a mixture of carbonate-based solvents. A representative electrolyte includes high-viscosity cyclic carbonates (*e.g.*, ethylene carbonate, EC) mixed with low-viscosity linear carbonates (*e.g.*, dimethyl carbonate, DMC; ethyl methyl carbonate, EMC) [19, 20]. EC, due to its high dielectric constant, promotes lithium salt dissolution and forms a stable SEI film on graphite anodes, making it widely used in commercial electrolytes [21, 22]. However, the high melting point of EC (36.4 °C) limits ion transport at low temperatures [23, 24]. In addition, its poor oxidative stability under high-temperature or high-voltage conditions leads to decomposition, generating harmful byproducts such as HF and CO_2, which pose significant safety concerns [25, 26].

To improve the wide-temperature performance of electrolytes, nitrile-based solvents have recently attracted considerable attention. These solvents exhibit high dielectric constant, low melting point, and high boiling point, showing great potential for wide-temperature electrolyte applications [27–29]. However, these applications are hindered by several challenges, including poor compatibility with lithium metal and graphite anodes, as well as safety concerns arising from the low flash points of short-chain nitriles [30–33]. These limitations can be addressed through strategies such as co-formulation with carbonate or ether solvents, the use of high-flash-point nitriles, the incorporation of functional additives, or interfacial engineering to improve the electrode–electrolyte compatibility [34–41].

Butyronitrile (BN), a representative nitrile solvent, combines several favorable characteristics: a low melting point (−112 °C), high boiling point (118 °C), low viscosity (0.515 cP at 25 °C), and high dielectric constant (20.7 at 25 °C), all of which contribute to efficient ionic transport under both low- and high-temperature conditions [42]. Moreover, the cyano group (C≡N) in BN provides good oxidative stability and can coordinate with metal ions from high-voltage cathodes, thereby suppressing side reactions and expanding the electrochemical stability window of the electrolyte [43–46]. Previous studies have shown that mixing BN with carbonates can effectively improve low-temperature performance [42]. Furthermore, the compatibility of BN with lithium metal and the stability of the solid electrolyte interphase can be enhanced by incorporating additives such as fluoroethylene carbonate (FEC) or designing dual-salt electrolyte systems, enabling excellent rate capability and cycling stability even at −40 °C [39, 46].

Currently, research on wide-temperature electrolytes mainly focuses on compositional design and performance optimization, while the temperature-dependent evolutions of their solvation structures and molecular dynamics remain underexplored. The solvation structure of lithium ions plays a vital role in determining ionic conductivity, electrochemical stability and interfacial properties, and is highly sensitive to factors such as solvent composition, salt concentration, and temperature [47]. Therefore, gaining a deeper understanding of how temperature affects the structural and dynamic properties of wide-temperature electrolytes is essential for guiding desired performance improvements.

In this work, we designed a BN-based wide-temperature electrolyte system composed of LiTFSI as the lithium salt and a co-solvent mixture of DMC and BN at a molar ratio of approximately 1:3:9 (Li^+:DMC:BN). Temperature-dependent infrared (IR) spectroscopy, employing carbonyl (C=O) and C≡N groups as structural probes, combined with molecular dynamics (MD) simulations and density functional theory (DFT) calculations, are used to systematically investigate the structural evolution and molecular dynamics of this electrolyte over a temperature range of −45 °C to 45 °C. High ionic conductivity was observed (*e.g.* 14.3 $mS\cdot cm^{-1}$ at 20 °C) for the mixed DMC/BN electrolyte. Our results reveal the microscopic mechanisms underlying the excellent wide-temperature performance of the designed systems studied in this work.

II. MATERIALS AND METHODS

A. Electrolyte preparation

LiTFSI (99%) was purchased from Energy Chemical, DMC (99.5%) from J&K, and BN (99%) from Aladdin. The mixed solvent was prepared by combining DMC and BN at a volume ratio of 1:3 without any lithium salt. The butyronitrile-based electrolyte (1 mol/L) was obtained by dissolving 28.8 mg of LiTFSI in the above

DOI: 10.1063/1674-0068/cjcp2507101

mixed solvent composed of 25 μL DMC and 75 μL BN. The molar ratio of components in this electrolyte was approximately Li^+:DMC:BN≈1:3:9. After preparation, the electrolyte was sonicated to enhance solvation and then left to stand for at least 48 h. No phase separation was observed during this period, indicating that the system was homogeneous and stable.

B. Temperature-dependent Fourier transform infrared (FTIR) spectroscopy

Temperature-dependent FTIR experiments were performed using a temperature-controlled transmission setup (Specac, UK) equipped with a vacuum jacket and a dewar-based cooling system. A 6 μm-thick spacer was inserted between the sample cell windows. Approximately 20 μL of electrolyte was filled between two CaF_2 windows without air bubbles, and the IR cell was sealed with vacuum grease. The temperature was controlled between −45 and 45 °C at a 5 °C increment. At each temperature stabilization point, an IR spectrum was collected with 64 scans. During the IR experiment, the sample chamber was continuously purged with dry nitrogen to avoid interference from ambient water moisture and CO_2.

C. Ionic conductivity measurement

Ionic conductivity measurements were conducted using a calibrated conductivity meter. The electrolytes, comprising 1 mol/L LiTFSI in pure DMC and in a DMC:BN (1:3, V/V) solvent mixture, were prepared in a fume hood. For each measurement, the electrolyte was temperature-controlled in a water bath, which was maintained at specific set points from ca. 0 °C to 40 °C using an ice/water mixture or heating as required, at a step of 10 °C. The conductivity cell was immersed in the sample, and the stabilized reading was recorded after thermal equilibrium was achieved. Each measurement was performed in triplicate at every temperature, and the average value was reported. The measurement was carried out using a commercial conductivity meter (Beijing Timepower Co.).

D. Quantum chemistry calculation

Density functional theory (DFT) calculations were performed at the B3LYP/6-31+G(d) level to optimize the geometries and obtain vibrational frequencies of individual molecules and molecular complexes, including DMC, BN, $TFSI^-$, DMC–Li^+, BN–Li^+, LiTFSI, DMC–BN, and Li^+. The HOMO and LUMO energy levels were analyzed using the Multiwfn wavefunction analysis program [48] and visualized with VMD software [49]. All DFT calculations were carried out using the polarizable continuum model (PCM) [50] to simulate the dielectric environment of the mixed solvent. The molar ratio of DMC to BN was set to 1:3, and the static and dynamic dielectric constants were 16.32 and 1.90, respectively. To obtain more accurate binding energies, single-point energy calculations using the high-level aug-cc-pVQZ basis set were performed for the interactions between Li^+ and DMC, BN, and $TFSI^-$. All calculations were conducted using the Gaussian 09 software package [51].

E. Molecular dynamics simulations

Molecular dynamics (MD) simulations were performed using the GROMACS software [52]. The OPLS-AA force field was used to describe both inter- and intramolecular interactions, and the force field parameters for all solvent molecules were generated via the LigParGen server [53–55]. The initial configurations were constructed using PACKMOL [56], by embedding the electrolyte molecules into a cubic box with a side length of 55 Å. During the MD process, a 2 ns NPT ensemble equilibration at 500 K was first carried out to pre-equilibrate the system and obtain a uniform single-phase initial configuration. This was followed by a 3 ns annealing process (NPT ensemble), during which the temperature was gradually reduced from 330 K to 298 K. Based on the equilibrated system, further simulations were conducted at 228 K and 318 K, respectively. At each temperature, a 10 ns NVT ensemble simulation was performed, followed by a 10 ns MD simulation in the NPT ensemble. The temperature and pressure were controlled using the Nose–Hoover thermostat and the Berendsen barostat, respectively. A time step of 1.0 fs was used throughout all simulations. From the MD trajectories, the radial distribution functions (RDFs), $g(r)$, of nitrogen atoms (N) in BN, carbonyl oxygen atoms (O) in DMC, and nitrogen (N) and oxygen atoms (O) in $TFSI^-$ with respect to Li^+ were extracted. Based on the RDFs, the corresponding coordination numbers (CNs) were further determined.

The primary objective of the MD simulations in this work was to elucidate the topological features of the Li^+ solvation structure and its evolution with temperature, rather than to assess absolute structural stability or

DOI: 10.1063/1674-0068/cjcp2507101

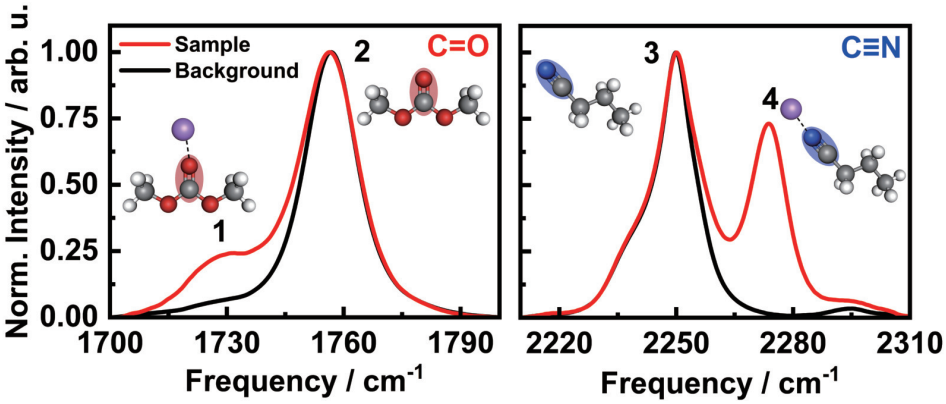

FIG. 1 FTIR spectra of the electrolyte (red) and the mixed solvent (black) in the C=O absorption region (left) and the C≡N absorption region (right). Four absorption peaks correspond to Li^+-coordinated C=O (peak 1), free C=O (peak 2), free C≡N (peak 3), and Li^+-coordinated C≡N (peak 4), respectively.

chemical reactions. The OPLS-AA force field was employed for its proven capability to describe intermolecular interactions and capture relative coordination trends. While this classical force field does not model bond breaking/forming, its results, specifically the temperature-dependent coordination numbers and RDFs, show excellent consistency with the trends observed in our variable-temperature FTIR experiments and are further supported by DFT binding energy calculations. This multi-technique agreement validates the use of MD for revealing the competitive coordination dynamics among BN, DMC, and $TFSI^-$ within the solvation shell across the studied temperature range.

III. RESULTS AND DISCUSSION

A. FTIR spectral analysis

FIG. 1 shows the intensity-normalized FTIR spectra of the electrolyte and its mixed solvent without lithium salt in the C=O and C≡N frequency regions at room temperature (ca. 25 °C). In the mixed solvent (black line), the frequency of the C=O stretching vibration of DMC appears at 1756.7 cm^{-1}, while the C≡N stretching vibration of BN is located at 2249.9 cm^{-1}. Upon the addition of LiTFSI (red line), the frequencies of the free C=O and C≡N absorption peaks remain almost unchanged. However, due to coordination with Li^+, the C=O peak redshifts to 1731.9 cm^{-1}, and the C≡N peak blueshifts to 2273.8 cm^{-1}. Therefore, in the butyronitrile-based electrolyte, four distinct absorption peaks are observed in the frequency regions of C=O and C≡N stretching vibrations, corresponding to Li^+-coordinated C=O (peak 1), free C=O (peak 2), free C≡N (peak 3), and Li^+-coordinated C≡N (peak 4), respectively.

The opposite shifts of the frequencies of the C=O and C≡N stretching vibrations upon coordination arise from their distinct electronic structural characteristics [57, 58]. In DMC, the C=O group serves as a strong electron acceptor. Coordination with Li^+ weakens its double-bond character, reducing the bond order and resulting in a red shift of the vibrational frequency. In contrast, the C≡N bond in BN has a relatively high electron density. Upon coordination with Li^+, the electron cloud becomes further polarized, increasing the bond force constant and causing a blue shift in frequency.

Topological electron density analysis of DMC and BN molecules and their Li^+ complexes further supports this explanation: the electron density of the C=O bond in isolated DMC is 0.4132 atomic unit (a.u.), which decreases to 0.4010 a.u. in the DMC–Li^+ complex. In contrast, the electron density of the C≡N bond in BN slightly increases from 0.4649 a.u. to 0.4655 a.u. This trend in electron density changes is highly consistent with the frequency shifts observed in the experimental spectra.

B. Temperature-dependent infrared spectroscopy

To further investigate the thermal stability of Li^+ coordination structures in the electrolyte and their response to the local solvent environment, temperature-dependent FTIR spectroscopy was measured over the range of −45 °C to 45 °C (FIG. 2). The results show that with increasing temperature, the absorption peak of Li^+-coordinated C=O undergoes a pronounced blue shift. The absorption peaks of free C=O and C≡N also exhibit slight blue shifts, while the Li^+-coordinated C≡N peak shows a red shift. This indicates that the vibra-

DOI: 10.1063/1674-0068/cjcp2507101

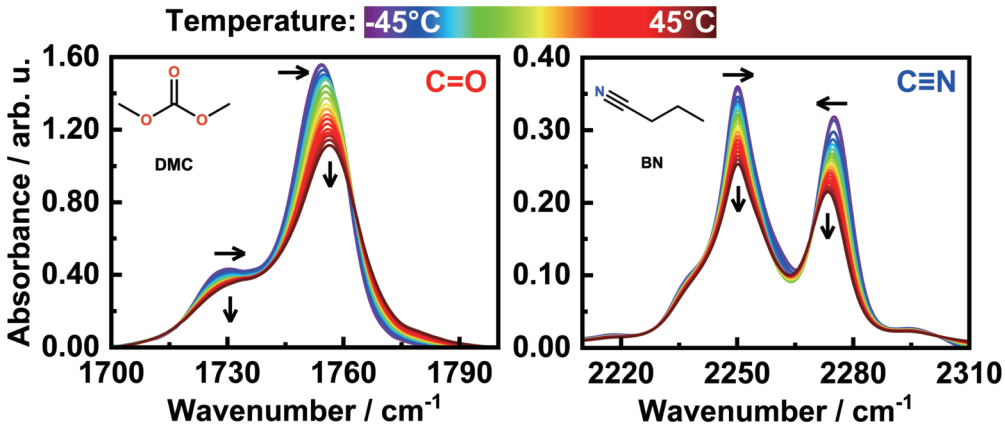

FIG. 2 Temperature-dependent FTIR spectra of the electrolyte in the C=O absorption region (left) and those in the C≡N absorption region (right). Arrows indicate the direction of changes of frequency and transition intensity from −45 °C to 45 °C.

tional modes of molecules in solution are highly sensitive to their local structural and solvent environments [59].

To clearly visualize the temperature response of each absorption band, the peak positions of C=O and C≡N at different temperatures were extracted and plotted as frequency shifts relative to those at −45 °C (FIG. 3). The results reveal that the vibrational frequency of the coordinated C=O exhibits the most significant blue shift with increasing temperature, followed by that of free C=O. However, the frequency of free C≡N remains nearly unchanged, whereas that of the coordinated C≡N shifts to lower wavenumbers (red shift). These differences in frequency shifts reflect the intrinsic differences in chemical environments and temperature sensitivities of the four vibrational probes.

Specifically, in free DMC molecules, dipole–dipole interactions or weak C=O···H–C interactions between carbonyl oxygen and methyl hydrogen atoms reduce the bond order of the C=O group. As temperature increases, these intermolecular interactions are weakened, enhancing the intrinsic bond strength and resulting in a blue shift of the C=O vibrational frequency. This trend is consistent with the commonly observed higher vibrational frequencies in the gas phase compared to the condensed phase. In the presence of Li^+, a typical ion–dipole coordination forms between Li^+ and carbonyl oxygen, significantly lowering the electron density of the C=O bond and inducing a red shift. However, as temperature increases, enhanced thermal motion likely increases the average Li^+–O distance, shortens the coordination lifetime, and increases dynamic fluctuations. As a result, the polarization effect on the C=O

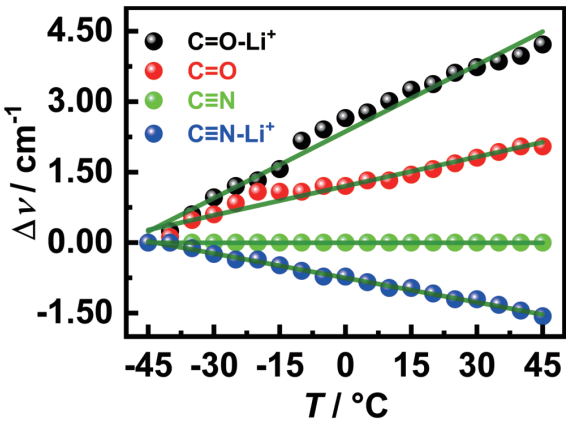

FIG. 3 Temperature-dependent frequency shifts of the C=O and C≡N vibrational probes.

bond weakens, partially restoring its bond strength and causing a corresponding blue shift in vibrational frequency.

In contrast, BN molecules interact predominantly through weak dipole–dipole forces, which exert a negligible influence on the strongly bonded C≡N triple bond. As a result, the vibrational frequency of free C≡N is largely insensitive to temperature. The coordination between Li^+ and the nitrogen atom of BN also involves ion–dipole interactions. At lower temperatures, this coordination enhances bond polarization and increases the force constant of the C≡N bond, producing a blue shift. As the temperature rises, the coordination bond weakens, partially restoring the bond order of the ligands and reducing their force constants, and hence resulting in a red shift of the corresponding vibrational frequency.

The above analysis demonstrates that increasing temperature generally weakens the coordination between Li^+ and solvent molecules, causing each vibra-

DOI: 10.1063/1674-0068/cjcp2507101

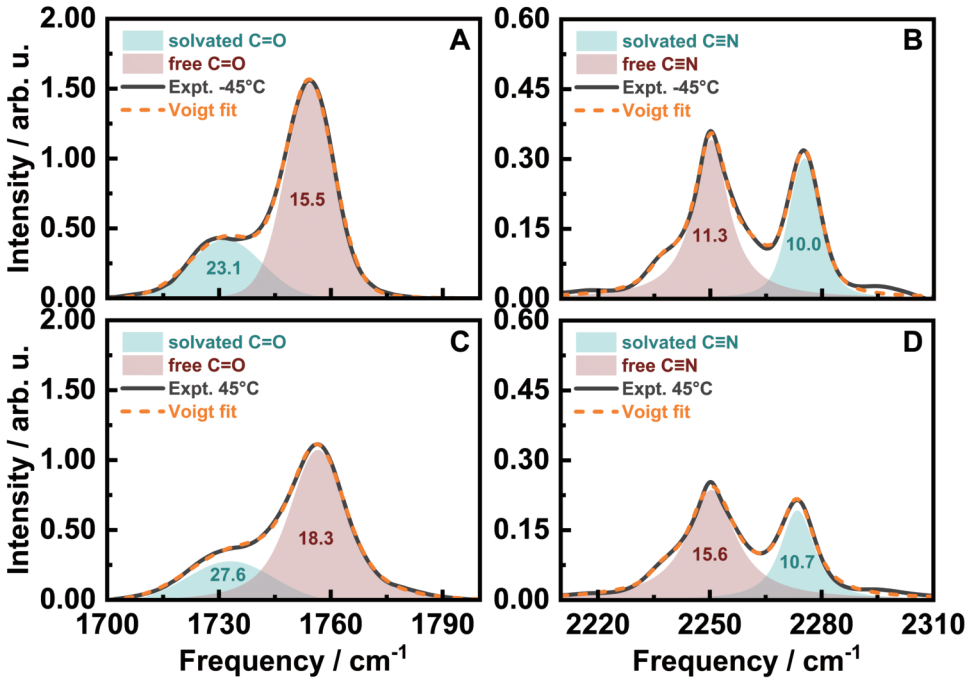

FIG. 4 FTIR spectra with Voigt function fittings of the butyronitrile-based electrolyte. (A) C=O absorption region at −45 °C; (B) C≡N absorption region at −45 °C; (C) C=O absorption region at 45 °C; (D) C≡N absorption region at 45 °C. Shaded values indicate the fitted full width at half maximum (FWHM).

tional probe to approach its free (non-bonded) state. This highlights the sensitivity of the C=O and C≡N vibrational modes to changes in the local chemical environment. Therefore, the C=O and C≡N groups can serve as effective vibrational probes for revealing the temperature-dependent evolution of solvation structures and the dynamic characteristics of corresponding Li^+ coordination complexes, demonstrating the practicality and sensitivity of these probes in mechanistic studies of electrolyte systems.

C. Temperature dependence of linewidth

The linewidth of an absorption peak not only reflects the energy distribution of a vibrational mode but also provides insights into the homogeneity of the molecular environment and associated dynamic behavior. In infrared spectroscopy, variations in linewidth serve as sensitive indicators of local structural fluctuations, intermolecular interactions, and the stability of coordination structures. Linewidth broadening can arise from intramolecular vibrational/rotational dynamics (homogeneous broadening) or from structural variations in heterogeneous microenvironments (inhomogeneous broadening). In solution systems, particularly those with complex solvation structures, inhomogeneous broadening is typically dominant.

FIG. 4 (A) and (B) show the experimental spectra and corresponding Voigt function fits at −45 °C. At this temperature, the linewidth of the Li^+-coordinated C=O absorption peak is 23.1 cm^{-1}, significantly broader than that of the free C=O peak at 15.5 cm^{-1}, indicating a more complex and heterogeneous coordination environment. In contrast, for the C≡N probe, the linewidth of the free-state absorption peak is 11.3 cm^{-1}, larger than that of the coordinated state (10.0 cm^{-1}), suggesting that BN molecules adopt a more ordered and spatially constrained configuration upon Li^+ coordination. FIG. 4 (C) and (D) present the FTIR spectra and Voigt function fitting results for C=O and C≡N stretching vibrations at 45 °C. As the temperature increases from −45 °C to 45 °C, the linewidth of the Li^+-coordinated C=O peak increases by approximately 4.5 cm^{-1}, while that of the Li^+-coordinated C≡N peak increases by only ~0.7 cm^{-1}. In contrast, the linewidths of the free C≡N and C=O peaks increase by ~4.3 cm^{-1} and ~2.8 cm^{-1}, respectively.

It is obvious that the Li^+-coordinated C=O exhibits the greatest temperature sensitivity, with its linewidth strongly influenced by thermal fluctuations, indicating a significant increase in the heterogeneity of the solvation shell structure with rising temperature. In contrast, the Li^+-coordinated C≡N peak shows a minimal re-

DOI: 10.1063/1674-0068/cjcp2507101

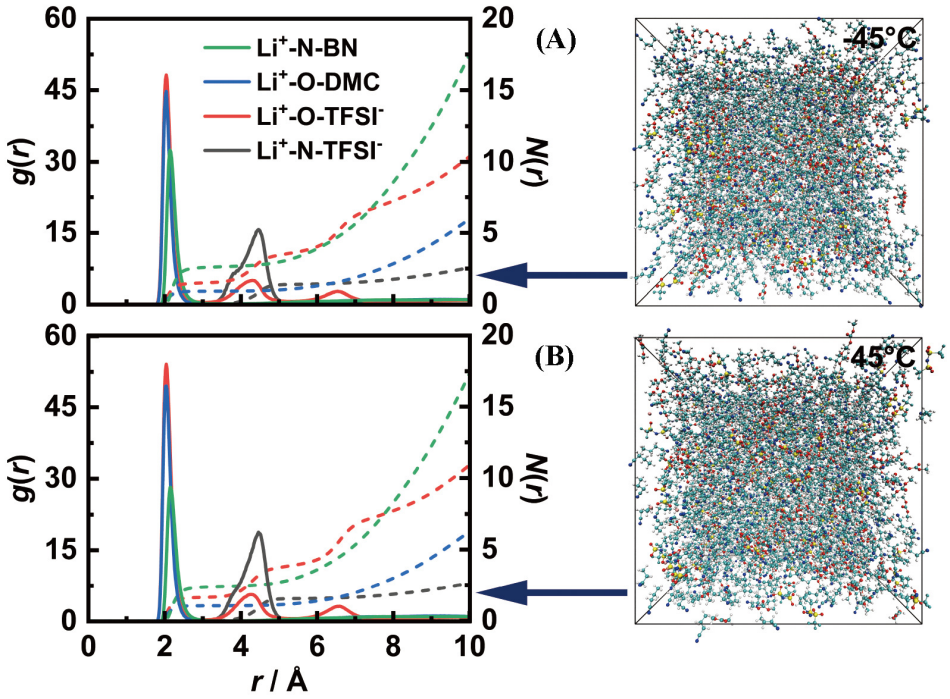

FIG. 5 RDF and CN profiles for Li–N/O$_X$ (X=BN, DMC, TFSI$^-$) pairs in the electrolyte at −45 °C (A) and 45 °C (B). Li–N/O$_X$ represents the radial distribution of nitrogen or oxygen atoms from solvent molecules or anions relative to Li$^+$. RDFs are shown as solid lines, and coordination numbers are shown as dashed lines.

sponse to the temperature change, suggesting that the coordination between BN and Li$^+$ is more stable and the local structure is less affected by thermal perturbation. For the free-state C=O and C≡N, increasing temperature enhances molecular thermal vibrations, contributing to both homogeneous and inhomogeneous broadening. In particular, the more pronounced broadening of the free C≡N peak may be attributed to intensified internal dynamics of the nitrile group. DMC molecules are surrounded by BN in the electrolyte, which is less disturbed by the microenvironment. As a result, the frequency distribution of the C=O stretching vibration is less affected by temperature. In contrast, free C≡N groups are more spatially dispersed, leading to greater sensitivity in vibrational frequency shifts.

Overall, the introduction of BN and its coordination with Li$^+$ contribute to the formation of a more ordered solvation structure, mitigating the impact of temperature on structural distribution and enhancing the overall thermal stability and ion transport order of the system. In particular, the low temperature sensitivity of the Li$^+$-coordinated C≡N absorption peak indicates that the BN-based solvation structure remains more stable and ordered across a wide temperature range. Combined with the analysis of primary solvation shell transport mechanisms, these findings highlight the critical role of BN in facilitating effective Li$^+$ migration within the electrolyte.

D. Structural dynamics from MD simulations

To investigate the solvation structure of Li$^+$ in the electrolyte system, MD simulations were performed at −45 °C and 45 °C. FIG. 5 shows the radial distribution functions ($g(r)$) and the corresponding coordination number ($N(r)$) for Li–N/O pairs at both temperatures. The first peaks and distinct minima around 2 Å in the RDF curves indicate that a relatively stable first solvation shell is formed around Li$^+$, and this solvation structure remains generally stable overall within the range of −45 °C to 45 °C, but still shows some temperature dependence. Table I lists the key parameters extracted from $g(r)$ and $N(r)$ in FIG. 5. The first major RDF peaks for Li–N$_{BN}$, Li–O$_{DMC}$, and Li–O$_{TFSI^-}$ appear at 2.16 Å, 2.04 Å, and 2.04 Å, respectively, indicating that Li$^+$ is co-solvated by BN, DMC, and TFSI$^-$. As temperature increases, the peak intensities ($g(r_{max})$) for Li–O$_{DMC}$ and Li–O$_{TFSI^-}$ increase, while that for Li–N$_{BN}$ decreases, suggesting that temperature affects both the distribution and coordination strength within the solvation shell. Coordination numbers obtained

DOI: 10.1063/1674-0068/cjcp2507101

TABLE I The key parameters extracted from $g(r)$ and $N(r)$ at −45 and 45 °C in FIG. 5. r_{max} and r_{min} (r in Å) represent the positions of the first maximum and minimum in $g(r)$, respectively. $g(r_{max})$ denotes the peak intensity at r_{max}, and $N(r_{min})$ represents the coordination number.

RDF pairs	r_{max}[a]		$g(r_{max})$		$N(r_{min})$	
	−45 °C	45 °C	−45 °C	45 °C	−45 °C	45 °C
Li–N_{BN}	2.16	2.16	32.09	28.17	2.52	2.32
Li–O_{DMC}	2.04	2.04	44.74	49.53	0.91	1.06
Li–O_{TFSI^-}	2.04	2.04	48.18	54.11	1.47	1.63

[a] r_{min} values of Li–N/O pair are the same, 2.70 Å, at −45 and 45 °C.

from the integrated $N(r_{min})$ functions further reveal that, as the temperature increases from −45 °C to 45 °C, the $N(r_{min})$ for BN decreases from 2.52 to 2.32, while those of DMC and $TFSI^-$ increase from 0.91 to 1.06 and from 1.47 to 1.63, respectively. These results further confirm that the coordination competition among BN, DMC, and $TFSI^-$ around Li^+ is temperature-dependent, leading to distinct solvation structures at low and high temperatures.

Overall, the butyronitrile-based electrolyte remains a stable solvation structure across a wide temperature range, facilitating efficient Li^+ transport. At higher temperatures, the solvation shell becomes more relaxed, which facilitates Li^+ desolvation and enhances interfacial reactivity. Additionally, the temperature-regulated solvation structure may influence the composition of SEI/cathode electrolyte interface (CEI) precursors. For example, the increased coordination of $TFSI^-$ at high temperatures may promote the formation of LiF-rich passivation layers, thereby improving the thermal stability and interfacial properties of the electrolyte.

E. Electrolyte performance estimation

To further understand the influence of individual components in the butyronitrile-based electrolyte on electrochemical performance, frontier molecular orbital analysis (HOMO and LUMO) was performed for DMC, BN, $TFSI^-$, and their Li^+ complexes, as shown in FIG. 6(A). Upon coordination with Li^+, the HOMO energy levels of both DMC and BN decrease significantly, indicating enhanced oxidative stability. BN–Li^+ exhibits the lowest HOMO level (–9.63 eV), suggesting the strongest resistance to oxidation, which contributes to improved high-voltage stability of the electrolyte. In contrast, $TFSI^-$ has the highest HOMO level

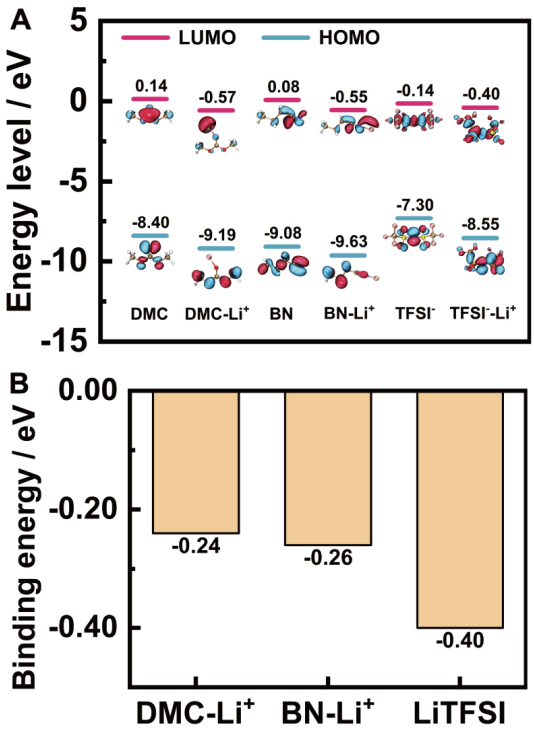

FIG. 6 (A) HOMO and LUMO energy level analysis, and (B) binding energy analysis.

(–7.30 eV), making it more susceptible to oxidation and thus a likely precursor for CEI formation, participating in the development of a LiF-rich cathode protective layer. In addition, the LUMO levels of DMC–Li^+, BN–Li^+, and $TFSI^-$–Li^+ are relatively similar, implying the possibility of cooperative reduction at the anode surface to form a composite SEI layer consisting of Li_2CO_3, LiF, and Li_3N. This cooperative interfacial film may effectively protect the anode surface and enhance its thermal stability.

FIG. 6(B) compares the binding energies of DMC, BN, and $TFSI^-$ coordinated with Li^+. The binding energies are –0.24 eV for DMC–Li^+, –0.26 eV for BN–Li^+, and –0.40 eV for $TFSI^-$–Li^+, with $TFSI^-$ exhibiting the strongest coordination strength. These values reflect the competitive interactions within the solvation structure. DMC, having the weakest interaction with Li^+, is more likely to dissociate from the solvation shell, whereas $TFSI^-$, with the strongest binding, especially at elevated temperatures, has a greater coordination advantage, resulting in a decreased proportion of BN in the solvation shell. This shift aligns well with the RDF and FTIR results, confirming that the solvation structure of Li^+ is thermally tunable: BN dominates at lower temperatures, while $TFSI^-$ becomes predominant at higher temperatures. This dynamic reorganization helps bal-

DOI: 10.1063/1674-0068/cjcp2507101

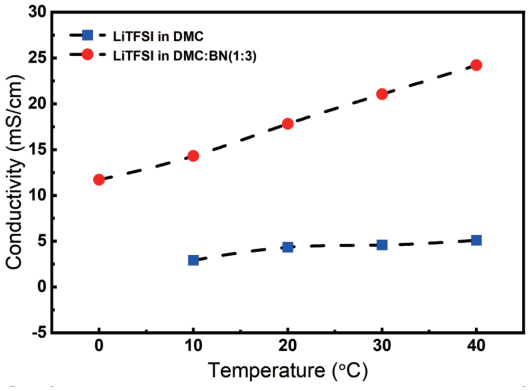

FIG. 7 Temperature-dependent ionic conductivity of LiTFSI in pure DMC and in the DMC:BN (1:3, V/V) mixed solvent.

ance the electrolyte's stability and functionality across a wide temperature range.

F. Ionic conductivity performance

To quantitatively evaluate the impact of butyronitrile (BN) on the macroscopic ion transport properties of the electrolyte, we systematically measured and compared the ionic conductivity of LiTFSI in pure DMC and in the DMC:BN (volume ratio of 1:3) mixed solvent over a temperature range of 0 °C to 40 °C, as shown in FIG. 7.

The introduction of BN significantly enhances the ion transport capability of the electrolyte across different temperatures.

The data unequivocally show that the conductivity of the DMC:BN-based electrolyte is significantly higher than that of the pure DMC system across the entire temperature range investigated. Crucially, at near room temperature (20 °C), the conductivity of the DMC:BN electrolyte reaches approximately 14.30 mS·cm^{-1}, substantially surpassing the 4.33 mS·cm^{-1} of the pure DMC system. As the temperature decreases, the conductivity of both systems decreases as expected; however, the DMC:BN system demonstrates superior retention at lower temperatures. For instance, at 10 °C, its conductivity remains at a high value of 14.30 mS·cm^{-1}, whereas the conductivity of the pure DMC system drops sharply to 2.90 mS·cm^{-1} at the same temperature.

Based on our deeper analysis, this performance enhancement can be attributed to BN's role in forming a more structured and ordered Li^+ solvation sheath. This ordered configuration reduces the activation energy for ion transport by facilitating a more coordinated and predictable migration pathway for Li^+. Concurrently, it promotes an efficient "structural diffusion" or hopping mechanism, where Li^+ can rapidly exchange between adjacent coordinating BN molecules, a process less hindered by viscosity at low temperatures. While the intrinsic low viscosity of BN aids fluidity, it is this fundamental restructuring of the solvation environment —creating a dynamic yet ordered coordination sphere —that primarily enables the superior ionic conductivity, particularly under challenging low-temperature conditions. These macroscopic results provide compelling evidence for the efficacy of BN-based electrolytes and direct our subsequent investigation into the underlying microscopic origins.

IV. CONCLUSION

In this work, temperature-dependent infrared spectroscopy, employing the C=O and C≡N stretching vibrations as probes, combined with molecular dynamics simulations and quantum chemical calculations, were used to investigate the temperature dependence and thermal reconstruction mechanism of the Li^+ solvation structure in a butyronitrile-based electrolyte. The results revealed distinct temperature dependences of these vibrational probes due to their different chemical environments: the coordinated C=O vibrational frequency showed a pronounced blue shift, that of free C≡N remained nearly unchanged, while that of coordinated C≡N displayed a red shift. These differences reflect the heterogeneous structural evolution of the solvation shell with temperature. The temperature dependence of the full width at half maximum further revealed changes in the microscopic dynamic environment. The observed spectral broadening with increasing temperature arose from both homogeneous broadening due to enhanced intramolecular vibrations and inhomogeneous broadening caused by intensified local environmental fluctuations. The temperature insensitivity of the coordinated C≡N absorption peak suggests that the formation of BN–Li^+ complexes may promote a more ordered solvation structure, thereby reducing thermal perturbation of the Li^+ coordination state and enabling efficient ion transport over a wide temperature range.

MD simulations revealed a temperature-dependent reconstruction mechanism of the primary Li^+ solvation shell. Within the temperature range of −45 °C to 45 °C, the electrolyte maintained a relatively stable solvation

DOI: 10.1063/1674-0068/cjcp2507101

structure. At low temperatures, Li^+ was primarily coordinated by BN, while at high temperatures, $TFSI^-$ became the dominant coordinating species, reflecting competitive coordination among solvent components and a temperature-regulated solvation mechanism. This tunable solvation structure helps optimize electrode–electrolyte interfacial behavior, particularly in modulating SEI/CEI formation under elevated temperatures.

DFT calculations showed that BN exhibits a moderate binding energy with Li^+ and the lowest HOMO level upon coordination, indicating excellent oxidative stability and enhanced high-voltage resistance of the electrolyte. $TFSI^-$ showed the strongest binding and highest HOMO level, making it more susceptible to oxidation and likely to contribute to Li-rich CEI formation. In contrast, DMC had the weakest binding energy and limited coordination ability. Analysis of LUMO levels suggested that BN, DMC, and $TFSI^-$ may synergistically contribute to the formation of a composite SEI layer enriched in Li_2CO_3, LiF, and Li_3N at the anode surface, thereby enhancing interfacial thermal stability.

In conclusion, we developed a BN-based wide-temperature electrolyte that demonstrates a significant enhancement in ionic conductivity across a broad temperature range compared to a conventional carbonate system. Microscopic structural analysis revealed that the origin of this performance lies in the stable yet dynamically tunable solvation structure facilitated by the cooperative interaction between BN and Li^+. This provides a microscopic foundation for wide-temperature operability and offers valuable theoretical and experimental guidance for electrolyte design and interfacial engineering.

V. ACKNOWLEDGMENTS

The work was supported by the National Natural Science Foundation of China (No.21603238 to Juan Zhao, Nos. 21573243 and 21327802 to Jianping Wang). The authors thank Ms. Zixin Liu at Institute of Chemistry Chinese Academy of Sciences for her help in measuring the ionic conductivity.

[1] A. Yoshino, Angew. Chem. Int. Ed. **51**, 5798 (2012).
[2] Q. Zheng, Z. Niu, J. Ye, S. Zhang, L. Zhang, L. Li, Y. Zhao, and X. Zhang, Adv. Funct. Mater. **27**, 1604299 (2017).
[3] Z. P. Cano, D. Banham, S. Ye, A. Hintennach, J. Lu, M. Fowler, and Z. Chen, Nat. Energy **3**, 279 (2018).
[4] Y. Liang, C. Z. Zhao, H. Yuan, Y. Chen, W. Zhang, J. Q. Huang, D. Yu, Y. Liu, M. M. Titirici, Y. L. Chueh, H. Yu, and Q. Zhang, InfoMat **1**, 6 (2019).
[5] J. Lindgren and P. D. Lund, J. Power Sources **328**, 37 (2016).
[6] Z. Zhang, C. Ji, Y. Liu, Y. Wang, B. Wang, and D. Liu, Batteries **10**, 107 (2024).
[7] S. S. Zhang, K. Xu, and T. R. Jow, Electrochim. Acta **49**, 1057 (2004).
[8] M. T. F. Rodrigues, G. Babu, H. Gullapalli, K. Kalaga, F. N. Sayed, K. Kato, J. Joyner, and P. M. Ajayan, Nat. Energy **2**, 17108 (2017).
[9] T. R. Jow, S. A. Delp, J. L. Allen, J. P. Jones, and M. C. Smart, J. Electrochem. Soc. **165**, A361 (2018).
[10] H. Saneifar, K. Zaghib, and D. Bélanger, ACS Appl. Energy Mater. **3**, 647 (2020).
[11] Q. Wang, P. Ping, X. Zhao, G. Chu, J. Sun, and C. Chen, J. Power Sources **208**, 210 (2012).
[12] Q. Li, S. Jiao, L. Luo, M. S. Ding, J. Zheng, S. S. Cartmell, C. M. Wang, K. Xu, J. G. Zhang, and W. Xu, ACS Appl. Mater. Interfaces **9**, 18826 (2017).
[13] D. Ouyang, K. Wang, J. Guan, and Z. Wang, J. Power Sources **607**, 234550 (2024).
[14] J. Wang, Q. Zheng, M. Fang, S. Ko, Y. Yamada, and A. Yamada, Adv. Sci. **8**, 2101646 (2021).
[15] T. Meng, S. Yang, Y. Peng, P. Li, S. Ren, X. Yun, and X. Hu, Adv. Energy Mater. 2404009 (2024).
[16] Q. Li, G. Liu, H. Cheng, Q. Sun, J. Zhang, and J. Min, Chemistry **27**, 15842 (2021).
[17] Y. Yang, W. Yang, H. Yang, and H. Zhou, eScience **3**, 100170 (2023).
[18] Y. K. Liu, C. Z. Zhao, J. Du, X. Q. Zhang, A. B. Chen, and Q. Zhang, Small **19**, 2205315 (2023).
[19] S. S. Zhang, T. R. Jow, K. Amine, and G. L. Henriksen, J. Power Sources **107**, 18 (2002).
[20] M. Li, R. P. Hicks, Z. Chen, C. Luo, J. Guo, C. Wang, and Y. Xu, Chem. Rev. **123**, 1712 (2023).
[21] K. Xu, Chem. Rev. **104**, 4303 (2004).
[22] C. Shen, S. Wang, Y. Jin, and W. Q. Han, ACS Appl. Mater. Interfaces **7**, 25441 (2015).
[23] M. C. Smart, B. V. Ratnakumar, L. D. Whitcanack, K. B. Chin, S. Surampudi, H. Croft, D. Tice, and R. Staniewicz, J. Power Sources **119–121**, 349 (2003).
[24] M. C. Smart, J. F. Whitacre, B. V. Ratnakumar, and K. Amine, J. Power Sources **168**, 501 (2007).
[25] L. Yang, B. Ravdel, and B. L. Lucht, Electrochem. Solid-State Lett. **13**, A95 (2010).
[26] L. Xia, B. Tang, L. Yao, K. Wang, A. Cheris, Y. Pan, S. Lee, Y. Xia, G. Z. Chen, and Z. Liu, ChemistrySelect **2**, 7353 (2017).
[27] Y. Yamada, K. Furukawa, K. Sodeyama, K. Kikuchi, M. Yaegashi, Y. Tateyama, and A. Yamada, J. Am. Chem. Soc. **136**, 5039 (2014).

DOI: 10.1063/1674-0068/cjcp2507101

[28] S. Tan, Z. Shadike, X. Cai, R. Lin, A. Kludze, O. Borodin, B. L. Lucht, C. Wang, E. Hu, K. Xu, and X. Q. Yang, Electrochem. Energy Rev. **6**, 35 (2023).
[29] L. Liu, Z. Shadike, X. Cai, M. Hong, Y. Gao, S. Shen, and J. Zhang, J. Mater. Chem. A **12**, 6947 (2024).
[30] A. M. Haregewoin, A. S. Wotango, and B. J. Hwang, Energy Environ. Sci. **9**, 1955 (2016).
[31] F. Qiu, X. Li, H. Deng, D. Wang, X. Mu, P. He, and H. Zhou, Adv. Energy Mater. **9**, 1803372 (2019).
[32] C. Kang, J. Zhu, Y. Wang, S. Ye, Y. Xiong, F. Kong, and G. Yin, Energy Storage Mater. **61**, 102898 (2023).
[33] F. Ivol, M. Porcher, A. Ghosh, J. Jacquemin, and F. Ghamouss, Molecules **25**, 2697 (2020).
[34] P. Isken, C. Dippel, R. Schmitz, R. W. Schmitz, M. Kunze, S. Passerini, M. Winter, and A. Lex-Balducci, Electrochim. Acta **56**, 7530 (2011).
[35] M. Kerner, D. H. Lim, S. Jeschke, T. Rydholm, J. H. Ahn, and J. Scheers, J. Power Sources **332**, 204 (2016).
[36] P. Hilbig, L. Ibing, M. Winter, and I. Cekic-Laskovic, Energies **12**, 2869 (2019).
[37] Y. Yang, Y. Yin, D. M. Davies, M. Zhang, M. Mayer, Y. Zhang, E. S. Sablina, S. Wang, J. Z. Lee, O. Borodin, C. S. Rustomji, and Y. S. Meng, Energy Environ. Sci. **13**, 2209 (2020).
[38] B. Zhu, X. Shi, T. Zheng, J. Xiong, Y. J. Cheng, and Y. Xia, Electrochim. Acta **425**, 140698 (2022).
[39] D. J. Yoo, Q. Liu, O. Cohen, M. Kim, K. A. Persson, and Z. Zhang, ACS Appl. Mater. Interfaces **14**, 11910 (2022).
[40] Z. Wang, Z. He, Z. Wang, J. Yang, K. Long, Z. Wu, G. Zhou, L. Mei, and L. Chen, Chem. Sci. **15**, 13768 (2024).
[41] O. J. Kim, Y. H. Cho, J. J. Kang, Y. S. Yu, C. Kim, and G. Y. Yun, Electron. Mater. Lett. (2024). https://doi.org/10.1007/s13391-024-00488-x
[42] Y. G. Cho, Y. S. Kim, D. G. Sung, M. S. Seo, and H. K. Song, Energy Environ. Sci. **7**, 1737 (2014).
[43] R. Rohan, T. C. Kuo, J. H. Lin, Y. C. Hsu, C. C. Li, and J. T. Lee, J. Phys. Chem. C **120**, 6450 (2016).
[44] S. Jiao, X. Ren, R. Cao, M. H. Engelhard, Y. Liu, D. Hu, D. Mei, J. Zheng, W. Zhao, Q. Li, N. Liu, B. D. Adams, C. Ma, J. Liu, J. G. Zhang, and W. Xu, Nat. Energy **3**, 739 (2018).
[45] X. Fan and C. Wang, Chem. Soc. Rev. **50**, 10486 (2021).
[46] J. Ning, K. Duan, K. Wang, J. Liu, S. Wang, and J. Zhang, J. Energy Chem. **67**, 290 (2022).
[47] Y. Lu, S. Yan, Y. He, Z. Liu, X. Ma, Y. Ou, W. Zhang, and K. Liu, Energy Storage Mater. **72**, 103741 (2024).
[48] T. Lu and F. Chen, J. Comput. Chem. **33**, 580 (2012).
[49] W. Humphrey, A. Dalke, and K. Schulten, J. Mol. Graph. **14**, 33 (1996).
[50] E. Cancès, B. Mennucci, and J. Tomasi, J. Chem. Phys. **107**, 3032 (1997).
[51] M. J. Frisch, G. W. Trucks, H. B. Schlegel, G. E. Scuseria, M. A. Robb, J. R. Cheeseman, G. Scalmani, V. Barone, B. Mennucci, G. A. Petersson, H. Nakatsuji, M. Caricato, X. Li, H. P. Hratchian, A. F. Izmaylov, J. Bloino, G. Zheng, J. L. Sonnenberg, M. Hada, M. Ehara, K. Toyota, R. Fukuda, J. Hasegawa, M. Ishida, T. Nakajima, Y. Honda, O. Kitao, H. Nakai, T. Vreven, J. A. Montgomery, Jr. , J. E. Peralta, F. Ogliaro, M. Bearpark, J. J. Heyd, E. Brothers, K. N. Kudin, V. N. Staroverov, R. Kobayashi, J. Normand, K. Raghavachari, A. Rendell, J. C. Burant, S. S. Iyengar, J. Tomasi, M. Cossi, N. Rega, J. M. Millam, M. Klene, J. E. Knox, J. B. Cross, V. Bakken, C. Adamo, J. Jaramillo, R. Gomperts, R. E. Stratmann, O. Yazyev, A. J. Austin, R. Cammi, C. Pomelli, J. W. Ochterski, R. L. Martin, K. Morokuma, V. G. Zakrzewski, G. A. Voth, P. Salvador, J. J. Dannenberg, S. Dapprich, A. D. Daniels, O. Farkas, J. B. Foresman, J. V. Ortiz, J. Cioslowski, and D. J. Fox, *Gaussian 09, Revision A. 02*, Pittsburgh PA: Gaussian, Inc., (2009).
[52] D. Van Der Spoel, E. Lindahl, B. Hess, G. Groenhof, A. E. Mark, and H. J. C. Berendsen, J. Comput. Chem. **26**, 1701 (2005).
[53] W. L. Jorgensen and J. Tirado-Rives, Proc. Natl. Acad. Sci. **102**, 6665 (2005).
[54] L. S. Dodda, I. Cabeza de Vaca, J. Tirado-Rives, and W. L. Jorgensen, Nucleic Acids Res. **45**, W331 (2017).
[55] L. S. Dodda, J. Z. Vilseck, J. Tirado-Rives, and W. L. Jorgensen, J. Phys. Chem. B **121**, 3864 (2017).
[56] L. Martínez, R. Andrade, E. G. Birgin, and J. M. Martínez, J. Comput. Chem. **30**, 2157 (2009).
[57] J. S. Seo, B. S. Cheong, and H. G. Cho, Spectrochim. Acta Part A Mol. Biomol. Spectrosc. **58**, 1747 (2002).
[58] N. Chapman, O. Borodin, T. Yoon, C. C. Nguyen, and B. L. Lucht, J. Phys. Chem. C **121**, 2135 (2017).
[59] K. E. Amunson and J. Kubelka, J. Phys. Chem. B **111**, 9993 (2007).

DOI: 10.1063/1674-0068/cjcp2507101